Electronic Supplementary Material (ESI) for Journal of Materials Chemistry A.

Electronic Supplementary Information

Zincophilic multilayer graphene structures levering fast and ultra-stable Zn-ion storage

Qi Huang [a], Yaowei Jin [a], Lu Huang [b], Yao Cong [a], Zijie Xu *[a]

[a]School of Chemical Science and Engineering, Tongji University, Shanghai, 200092, P. R. China.

[b]Department of Stomatology, Hangzhou Ninth People's Hospital, Hangzhou, 311225, P. R. China.

*E-mail: xzj@tongji.edu.cn (Z. Xu)

Section S1. Experimental Procedures

1.1 Materials.

Filter papers. NaCl (AR), HNO_3 (AR), sodium metal (CP), aqueous $Zn(CF_3SO_3)_2$ (AR) and $Fe(NO_3)_3 \cdot 9H_2O$ (AR) were all purchased from Sinopharm Chemical Reagent Co., LtdS.

1.2 Preparation of Amorphous Carbons.

$Fe(NO_3)_3 \cdot 9H_2O$ (4.03 g) was added in deionized water (20 mL) at 80 °C, and 5 g filter paper was soaking into it overnight to absorb iron salt. Then, previously soaked mixture was slowly poured into the 55 mL deionized water at 80 °C and stirred until forming paper pulp. After cooling, the paper pulp was sonicated for 30 minutes to fully disperse and was freeze-dried in a lyophilizer. After that, the obtained sample was ground into powder and heated at 700 °C for 2 h with a rate of 3 °C min^{-1} to get carbonized sample. The resultant carbon materials were marked with Fe-*x*, where *x* referred to molar mass. As for the reference sample, the starch was treated following the same process but without $Fe(NO_3)_3 \cdot 9H_2O$. The resulted sample was named as Fe-0. Thus, the sample with 2.01 g, 4.03 g and 20.15 g $Fe(NO_3)_3 \cdot 9H_2O$ were named as Fe-0.005, Fe-0.01 and Fe-0.05, respectively.

1.3 Preparation of Multilayer Graphene Structure in Amorphous Carbons.

0.20 g Fe-0.01 and 1.60 g NaCl were ground together, and 0.20 g sodium metal was carefully cut into particles, and the particles were evenly spread on the mixed sample, and then they were heated at 700 °C under N_2 atmosphere with a heating rate of 3 °C min^{-1}. After obtaining the morphological characteristics, X-ray diffraction angle and Raman spectra, the carbonized sample was washed in 2M HNO_3 and dried at 80 °C before the final electrochemical test. The resultant sample were marked with Fe-*x*-Na-*y*, where *x* referred to molar mass of iron salt, *y* referred to mass ratio of amorphous carbon obtained last step and sodium metal. Thus, the sample was marked as

Fe-0.01-Na-1:1(Fe-Na-1:1). According to the above step, the sample with 0.4 g sodium metal was marked as Fe-0.01-Na-1:2(Fe-Na-1:2), and the sample with 0.6 g sodium metal was marked as Fe-0.01-Na-1:3(Fe-Na-1:3).

1.4 Characterizations.

The microstructure was observed by JEM–2100 transmission electron microscope (TEM). Chemical composition and crystalline structure of carbon materials were measured by X-ray powder diffraction technique (XRD, Bruker D8 advance diffractometer). Raman spectra (Renishaw Invia) was investigated at an excitation wavelength of 514 nm to measure the graphitization degree of carbon materials. After above investigations, all samples have been washed in acid to remove the impurities. N_2 adsorption/desorption isotherms were achieved by an analyzer (Micromeritics) of ASAP 2460. The Brunauer-Emmett-Teller (BET) method was used to calculated the specific surface area and pore size.

1.5 Electrochemical Measurements.

Before electrochemical measurement, all the sample has been washed *via* 2 M HNO_3 and dried at 80 °C. The working electrode mixed by resulted sample, graphite and PTFE in the ratio of 8:1:1 was made into thin wafer with a diameter of 5 nm. Above mixture was soaked in ethanol and dispersed in ultrasound for 2 h, then dried at 100 °C in the vacuum drying oven for 12 h and weighed. Carbon//$Zn(CF_3SO_3)_2$//Zn hybrid supercapacitor was assembled in 2032 coin-type cell with the as-prepared carbon electrode as cathode, Zn foil anode and 3 M $Zn(CF_3SO_3)_2$ as electrolyte, while a glassy fibrous was used as separator in Zn ion hybrid capacitors.

Galvanostatic charging/discharge (GCD) was measured on the LAND-CT3001A battery test system with a potential range from 0 to 1.8 V. Cyclic voltammetry (CV) and electrochemical impedance spectroscopy (EIS) were investigated on the electrochemical workstation (CHI660E).

EIS was performed in the frequency range from 0.01 to 1,000 kHz. For the DRT calculation, the open Matlab code shared online by Prof. Francesco Giucci.[1, 2] The DRT analysis is a method to the deep investigation of EIS measurement. The distribution function of relaxation times depicts the time relaxation characteristics of the electrochemical workstation obtained. The DRT partitions the electrochemical process within different time constant (τ), showing the immediate method to the distribution of timescale. On account of the Tikhonov regulation and the regulation indexes is 0.001 in calculations.[3, 4] The range of DRT matching is based on the frequency range from 100 kHz to 0.01 Hz after the Kramers-Kronig validaty test. The specific capacity (C_m, mA h g^{-1}) and cycling performance were also evaluated on a LAND-CT3001A multichannel galvanostat within the voltage range of 0−1.8 V.

The gravimetric capacitance (C_{three}, C_{two} F g^{-1}) of the working electrode is computed according to the following equation:

$$C_{three} = \frac{I \times \Delta t}{m \times \Delta V} \quad \text{(Eq. S1)}$$

$$C_{two} = \frac{4 \times I \times \Delta t}{m \times \Delta V} \quad \text{(Eq. S2)}$$

where I (A g^{-1}), Δt (s), m (g), ΔV (V) is the current density, the discharge time, the total mass of sample electrodes and the voltage window, respectively.

The energy density (E) and power density (P) are calculated by the following equations:

$$E = C_m \times \Delta V \quad \text{(Eq. S3)}$$

$$P = \frac{C_m \times \Delta V}{1000 \times \Delta t} \quad \text{(Eq. S4)}$$

where ΔV is the voltage window.

Section S2. Supplementary Methods

2.1 Zn-Anode Utilization.

The utilization (%) of Zn anode is calculated based on the mass of consumed Zn foil (m_{Zn}, g cm^{-2}) after charge/discharge process and the initial mass of Zn anode ($m_{initial\ Zn}$, 0.074 g cm^{-2}), calculating by the following form:

$$\text{Utilization (\%)} = m_{Zn}/m_{initial} \times 100 \quad \text{(Eq. S5)}$$

The m_{Zn} is collected with the discharge capacity (C, mAh cm^{-2}) and the theoretical capacity of Zn anode (C_{Zn}, 820 mAh g^{-1}) based on the following equation:

$$C = m_{Zn} \times C_{Zn} = m_{carbon} \times C_{carbon} \quad \text{(Eq. S6)}$$

where C denotes on the mass loading of carbon materials on the cathode (m_{carbon}, g cm^{-2}) and corresponding specific capacity (C_{carbon}, mAh g^{-1}).

2.2 Electrochemically Active Surface Area.

The electrochemical active surface area (ECSA) is calculated through the following equation:

$$i_c = C_{dl} \times v \quad \text{(Eq. S7)}$$

$$\text{ECSA} = \frac{C_{dl}}{C^*} \quad \text{(Eq. S8)}$$

where i_c and v is the capacitive cathodic/anodic current (mA) and scan rate (V s^{-1}), respectively. And C_{dl} is equal to the slope of i_c –v curve, C^* is a specific capacitance constant (40 μF cm^{-2} in 1 M KOH). Assuming capacitance between 0.8–0.9 V can represent electrical double-layer capacitance, i_c and v are acquired from CV measured at different scan rates between 0.8–0.9 V *vs*. Ag/AgCl. Note: The specific capacitance constant of KOH solution is typically selected to

calculate the electrochemical active surface area, such as *J. Am. Chem. Soc.*, 2013, 135, 16977−16987.

2.3 Optical Energy Gap.

The optical energy gaps (E_g, eV) of carbon cathodes can be obtained by the ultraviolet-visible (UV-Vis) spectroscopy, which is expressed as:

$$\alpha \propto (h\nu - E_g)^{0.5}/h\nu \quad \text{(Eq. S9)}$$

$$h\nu = 1280/\lambda \quad \text{(Eq. S10)}$$

where α represents the optical absorption coefficient $h\nu$ is the photon energy, λ is the wavelength.

2.4 Activation Energy.

The activation energy (E_a, kJ mol^{-1}) for the charge transfer process can be deduced using the following Arrhenius equation:

$$R_{ct}^{-1} = A\exp(-E_a/\mathrm{RT}) \quad \text{(Eq. S11)}$$

where R_{ct} is the charge transfer resistance (Ω), A is constant under a stable experimental condition, R represents the gas constant (8.314 J mol^{-1} K^{-1}), and T is Kelvin temperature (K). The In (R_{ct}^{-1}) values are plotted *vs.* 1000/T, and linear fitting is calculated to get E_a:

$$\mathrm{In}\,(R_{ct}^{-1}) = -E_a/\mathrm{RT} + k \quad \text{(Eq. S12)}$$

where k is constant.

2.5 Ion Diffusion Behavior.

The relaxation time constant (τ_0, s) is collected from the reciprocal of the frequency (f, Hz):

$$\tau_0 = 1/f \quad \text{(Eq. S13)}$$

The ion transport resistivity (σ, Ω s$^{-0.5}$) and diffusion coefficient (D, cm^2 s^{-1}) were investigated by EIS spectra according to the following equations:

$$Z' = \sigma\omega^{-0.5} + R_s + R_{ct} \quad \text{(Eq. S14)}$$

And the ion diffusion coefficient (D, $cm^2\ s^{-1}$) is calculated by equation as follows:

$$D = \frac{R^2T^2}{2A^2C^2F^4n^4\sigma^2} \quad \text{(Eq. S15)}$$

where R (8.314 J $mol^{-1}\ K^{-1}$) is gas constant, T (293.15 K) is Kelvin temperature, A ($m^2\ g^{-1}$) is the surface area of electrodes, C (mol L^{-1}) is molar concentration of electrolyte, n is Faraday constant and σ ($\Omega\ s^{-0.5}$) is diffusive resistance.

2.6 Charge Storage Kinetics.

The relationship of total electrode capacitance (C_T), electrical double-layer capacitance (C_E), pseudocapacitance (C_P) and the fast dynamic calculation can be described by the following equation:

$$C_T = C_E + kt^{0.5} \quad \text{(Eq. S16)}$$

$$I = kv^b \quad \text{(Eq. S17)}$$

$$I = k_1v + k_2v^{0.5} \quad \text{(Eq. S18)}$$

$$Iv^{-0.5} = k_1v^{0.5} + k_2 \quad \text{(Eq. S19)}$$

where v (mV s^{-1}), b, k_1v, $k_2v^{1/2}$ is the scan rate, the power-law exponent, the current density contributed by fast-kinetic processes and the current density contributed by slow-kinetic processes, respectively.

2.7 Density Functional Theory.

Reduce Density Gradient (RDG): The theoretical calculations were conducted *via* the Gaussian 16W and Gauss View 6.0. The graphene/Zn-ion complex structure was optimized at the *wb*97XD/6-31+G(d) level of theory. The graphene edge was coordinated with H atoms. The RDG analysis was performed with Multiwfn program, where RDG values of sign $(\lambda_2)\rho$ is symbol of attractive interactions, value near zero implies weak interactions.[5] Additionally, the corresponding

gradient isosurface was colored, which is able to show the interaction region and intensity. The noncovalent interaction (NCI) maps were plotted through VMD software.

Adsorption Energy (ΔE_a): The first-principles simulations of all structural models on account of density functional theory (DFT) method were carried out by the Vienna Ab-initio Simulation Package (VASP). The electron exchange-correlation interactions were simulated by the projector augmented wave (PAW) pseudopotentials with a plane-wave cutoff of 520 eV and Perdew-Burke-Ernzerhof (PBE) functional within the generalized gradient approximation. The convergence tolerances of energy and force is set to 1×10^{-5} eV and 0.02 eV $Å^{-1}$. The geometry optimization was proceeded by the 3×3×1 Monkhorst-Pack k-point mesh. The adsorption energy was obationed through the following formula:

$$E_{ads} = E_{Zn/carbon} - E_{carbon} - E_{Zn} \quad \text{(Eq. S20)}$$

where $E_{Zn/carbon}$, E_{carbon}, and E_{Zn} is the energies of carbon systems with and without Zn adsorption, and the energy of single Zn atom in bulk structure, respectively. A more negative adsorption energy value reveals the stronger adsorption capability of the Zn ion on the carbon framework.

Charge Density Difference ($\Delta\rho$): To analyze the bonding nature of Zn adsorbed on the dual doped carbon framework and charge transfer index between them detailly, the charge density differences of Zn absorbed on the fabricated carbon structures were obtained by calculating the charge densities of the Zn atom and carbon matrix from the corresponding compounds.

$$\Delta\rho = \rho_{H/carbon} - \rho_{H} - \rho_{carbon} \quad \text{(Eq. S21)}$$

2.8 Finite Element Simulations.

To unravel the fundamental mechanism of Zn^{2+} ion transport process in Fe-Na based ZHCs, CFD simulations were carried out through COMSOL Multiphysics software with the “Tertiary Current Distribution” and “Phase Field” module.[6] A battery-column model was fabricated,

representing the theoretical structure of Fe-Na based ZHCs. The size of the entire two-dimension model for ion transport process in battery-column was set as 1.0 × 4.0 cm. The ion diffusion process within Fe-Na electrodes can be modeled and computed by the following Poisson-Nernst-Planck equations:

$$\nabla \cdot (D\nabla c_i + \frac{Dz_i e}{k_B T} c_i \nabla V) = 0 \quad \text{(Eq. S22)}$$

where c, D, z, e, k_B and T denote the ion concentration, the diffusion coefficient, the ion valence, the elementary charge, the Boltzmann constant, and the absolute temperature, respectively. The mentioned equations were solved in a time-dependent state to realize a steady state. In this work, to guarantee the high accuracy of the simulation outcome, the densest conventional triangular meshes were utilized for all simulations in the column. The MUMPS solver was used with a corresponding tolerance of 0.001.

The ion transport by the concentration diffusion in porous electrode model was set as 3.0 × 6.0 mm in an area filled with electrolyte following the Fick's law:

$$\mathbf{N}_i = \mathbf{J}_i = -D_i \nabla c_i \quad \text{(Eq. S23)}$$

$$\frac{\partial c_i}{\partial t} + \nabla \cdot \mathbf{J}_i = \mathrm{R}_{i,\,tot} \quad \text{(Eq. S24)}$$

where $\mathbf{J}_i$ is the ion flux, D_i is the diffusion coefficient of electrolytes, c_i is the ion concentration of electrolytes, ∇c_i is concentration gradient.

The relationship between the diffusion coefficient and electric mobility obeying the Nernst-Einstein equation:

$$\mathbf{N}_i = -D_i \nabla c_i - z_i u_{m,i} F c_i \nabla \phi_l + \mathbf{u} c_i = \mathbf{J}_i + \mathbf{u} c_i \quad \text{(Eq. S25)}$$

where z_i is the transport number ($z_{Zn} = 2$), $u_{m,i}$ is the electric mobility coefficient, F is the Faraday constant (96485 C mol^{-1}), ϕ is the electrolyte potential. And the equilibrium potential of the

electrode surface obeys the Nernst equation as following formula:

$$E_{eq} = -\frac{\Delta G}{nF} \quad \text{(Eq.S26)}$$

$$E_{eq} = E_{eq,ref} - \frac{RT}{nF} \ln \prod_i \left(\frac{\alpha_i}{\alpha_{i,ref}}\right)^{v_i} \quad \text{(Eq.S27)}$$

where E_{eq} is the electrode potential, $E_{eq,ref}$ is the standard electrode potential, ΔG is the Gibbs free energy, R is the ideal gas constant, T is the Kelvin temperature, n is the transfer electron number of the reaction, α_i is the electrode reactive ion concentration, $\alpha_{i,ref}$ is the standard electrode reactive ion concentration, v_i is the reaction stoichimometric number.

The electrode reaction for the electrode surface abides by the Butler-Volmer kinetics expression, as displayed in following formula:

$$i_{loc} = i_0 \left(\exp\left(\frac{\alpha_a F \eta}{RT}\right) - \exp\left(\frac{-\alpha_a F \eta}{RT}\right)\right) \quad \text{(Eq. S28)}$$

where i_{loc} is the local current density at the electrode/electrolyte interface, i_0 is the exchange current density, α_a and α_c is the anodic and cathodic charge transfer coefficients, η is the activation overpotential.

Section S3. Supplementary Characterizations

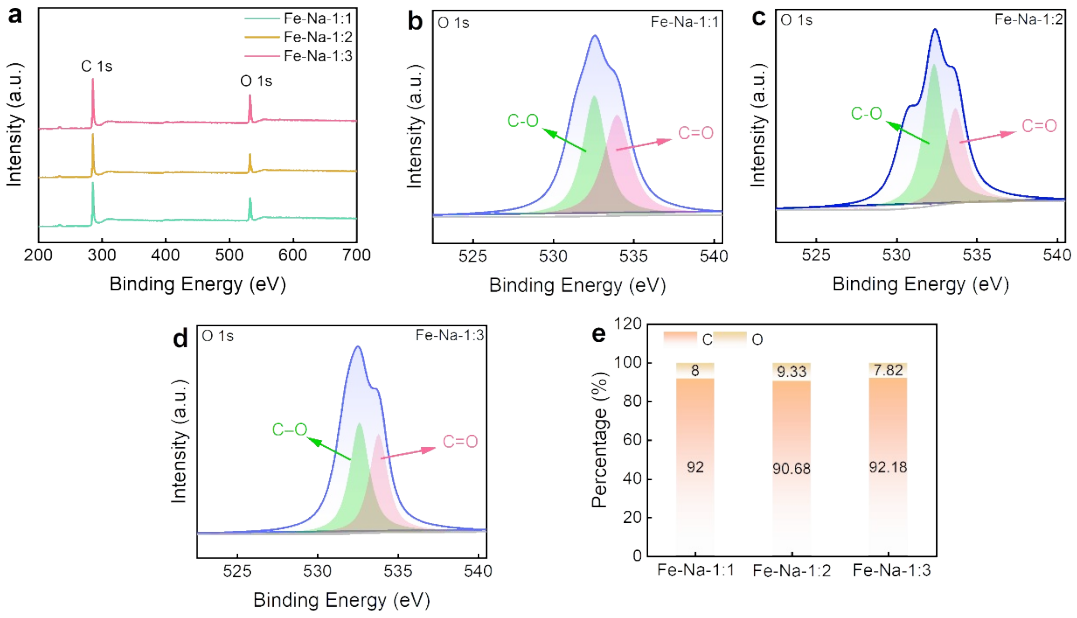

Fig. S1 XPS survey spectra of resulted samples derived from the same amorphous carbon with different sodium metal treatment, (a) XPS survey profiles of Fe-Na and high-resolution O 1s XPS spectrum of (b)Fe-Na-1:1, (c) Fe-Na-1:2, (d) Fe-Na-1:3. (e) C, O percentage of various samples.

Table S1. Pore structure parameters of Fe-Na samples.

Sample	S_{BET} ($m^2 g^{-1}$)	S_{micro} ($m^2 g^{-1}$)	S_{meso} ($m^2 g^{-1}$)	V_{total} ($cm^3 g^{-1}$)	V_{meso} / V_{total} (%)
Fe-Na-1:1	1343	1070	273	1.20	20.3
Fe-Na-1:2	1720	1192	528	2.18	30.7
Fe-Na-1:3	1137	982	155	1.07	13.6

S_{BET}, S_{micro}, S_{meso}, V_{total} and V_{meso} represents surface areas, micropore surface areas, mesopore surface areas, total pore volumes, mesopore volumes, respectively.

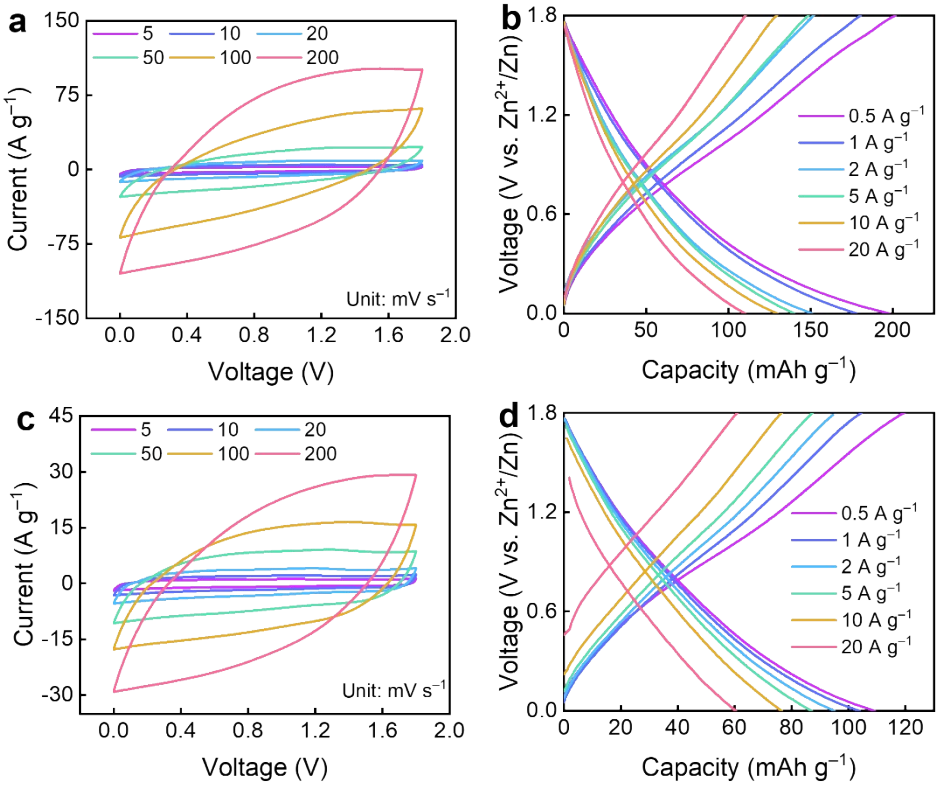

Fig. S2 Electrochemical performances of Fe-Na electrodes: (a) CV curves of Fe-Na-1:1, (b) GCD file of Fe-Na-1:1, (c) CV curves of Fe-Na-1:3 and (d) GCD file of Fe-Na-1:3.

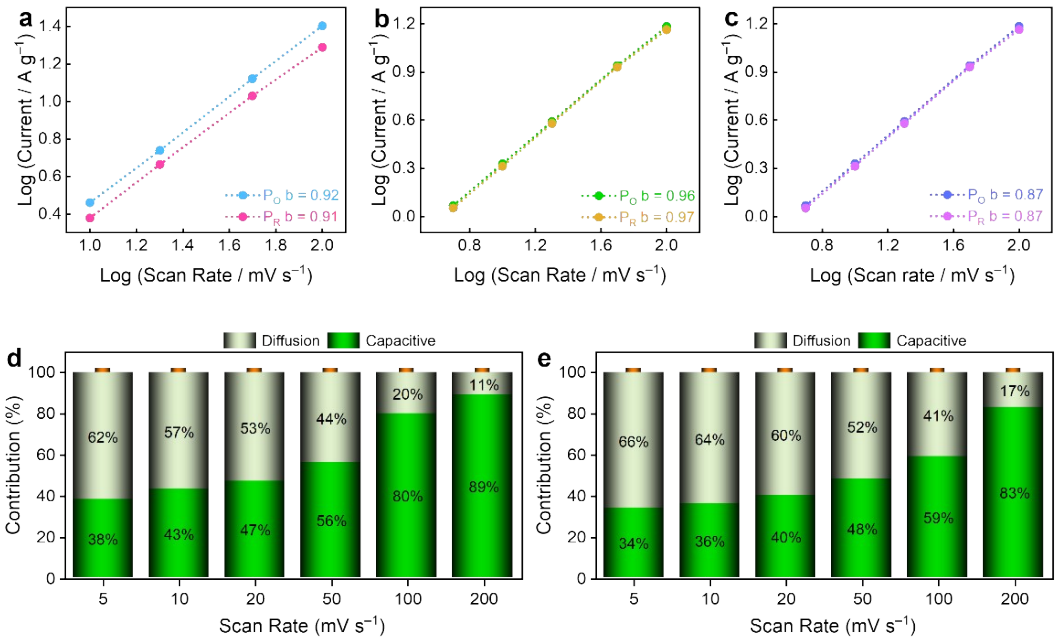

Fig. S3 (a–c) b values in the anodic and cathodic of Fe-Na-1:1, Fe-Na-1:2 and Fe-Na-1:3. (d, e) Capacitive and diffusion-controlled ratios of Fe-Na-1:1 and Fe-Na-1:3.

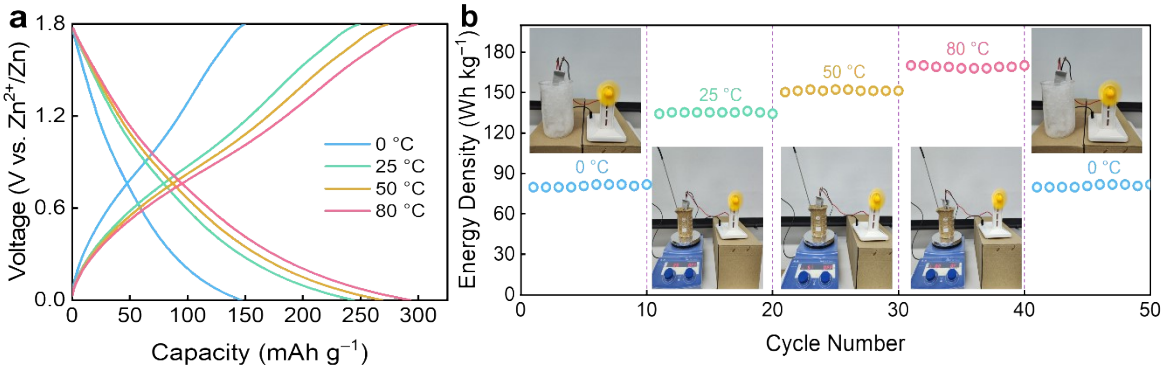

Fig. S4 (a) Voltage-capacity profiles and (b) energy densities of the Fe-Na device under temperature conditions (inset shows the photograph of a fan powered by the device).

Table S2. Comparison of electrochemical kinetics parameters of Fe-Na-based ZHCs

Device	E_g (eV)	E_{a1} (kJ mol^{-1})	E_{a2} (kJ mol^{-1})	R_s (Ω)	R_{ct} (Ω)	τ (s)	σ (Ω s$^{-0.5}$)	$D_{Zn^{2+}}$ (cm^2 s^{-1})
Fe-Na-1:1	2.91	3.2	13.1	1.14	17.1	6.8	16.9	2.71×10^{-7}
Fe-Na-1:2	2.74	1.8	9.4	0.7	9.4	4.6	6.5	1.72×10^{-6}
Fe-Na-1:3	3.32	5.3	17.4	1.7	25	7.1	21.8	1.42×10^{-7}

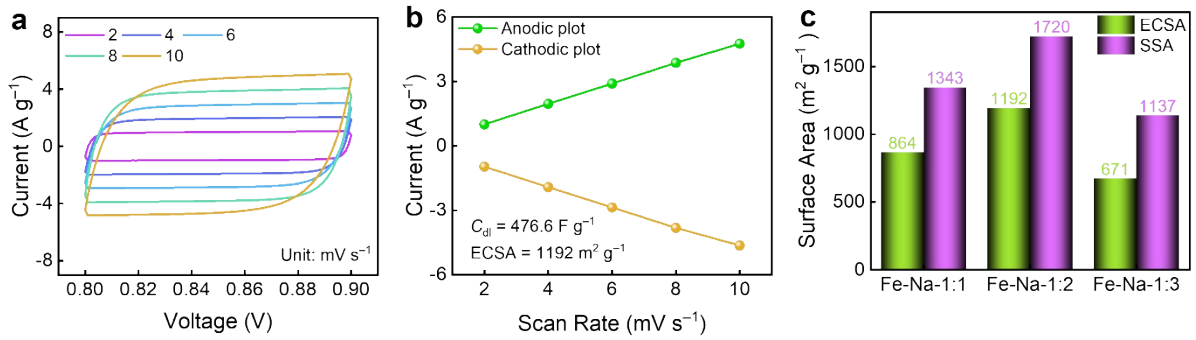

Fig. S5 (a) CV curves of Fe-Na-1:2 based ZHCs at different scan rates. (b) Cathodic/anodic charging current densities of Fe-Na-1:2 based ZHCs measured at 0.85 V plotted as a function of scan rate. (c) ECSA and SSA within various Fe-Na electrodes.

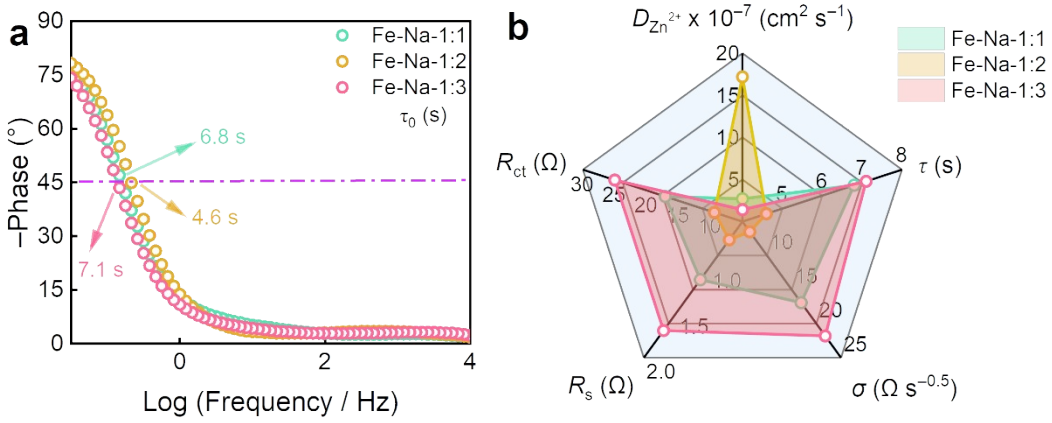

Fig. S6 (a) Bode plots. (b) Five contrasts of all devices.

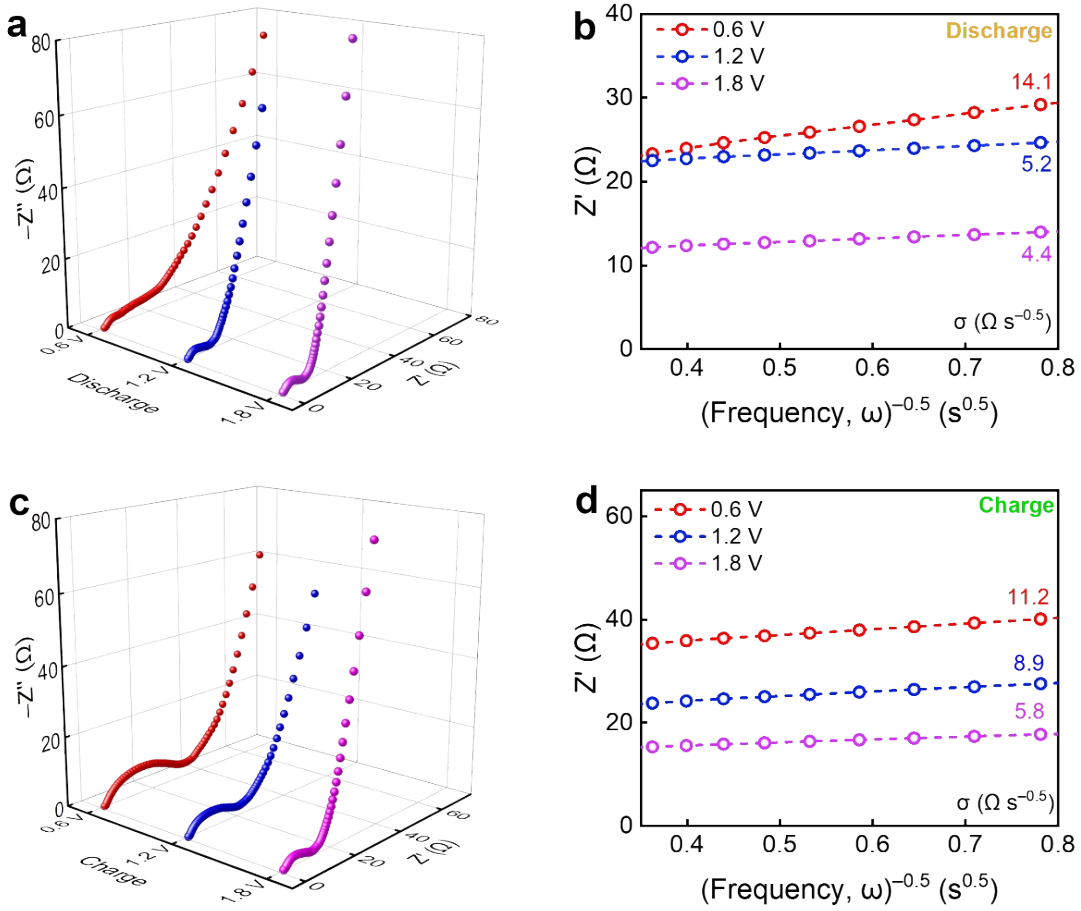

Fig. S7 (a, c) Spatial distribution of EIS curves of Fe-Na-1:2-loaded ZHCs at various discharge/charge process. (b, d) Randles plots of Fe-Na electrodes in dynamic charge/discharge process.

Table S3. Comparison of specific capacity (C_m), energy density (E), and capacity retention after cycling of recently reported carbon-based ZHCs in the literatures.

Materials	C_m (mAh g^{-1})	E (Wh kg^{-1})	Cycling Lifespan (%)	Refs.
MLG in amorphous carbon	278@0.2 A g^{-1} 115@100 A g^{-1}	148.9	92.9%, 300,000 cycles, 10 A g^{-1} 99.1%, Coulomb efficiency	This work
MOF-derived carbon	49.8@0.05 A g^{-1} 24.9@5 A g^{-1}	58.1	100%, 9,000 cycles, 1 A g^{-1}	[S7]

Carbon cages	225@0.1 A g^{-1} 71@20 A g^{-1}	97	96.5%, 300,000 cycles, 50 A g^{-1}	[S8]
Carbon nanofibers	136@0.1 A g^{-1} 57@50 A g^{-1}	98.3	99.2%, 200,000 cycles, 40 A g^{-1}	[S9]
Porous carbon	179.8@0.1 A g^{-1} 78.4@20 A g^{-1}	104.8	99.2%, 30,000 cycles, 20 A g^{-1}	[S10]
N-doped carbon	98@0.1 A g^{-1} 61@20 A g^{-1}	82	100%, 30,000 cycles, 5 A g^{-1}	[S11]
Pitch-derived carbon	136.2@0.3 A g^{-1} 69.2@15 A g^{-1}	81.1	98.9%, 60,000 cycles, 10 A g^{-1}	[S12]
Layered carbon	127.7@0.5 A g^{-1} 42.8@20 A g^{-1}	86.8	81.3%, 6500 cycles, 5 A g^{-1}	[S13]
Activated graphene	112@0.1 A g^{-1} 55@20 A g^{-1}	106.3	93%, 80,000 cycles, 8 A g^{-1}	[S14]

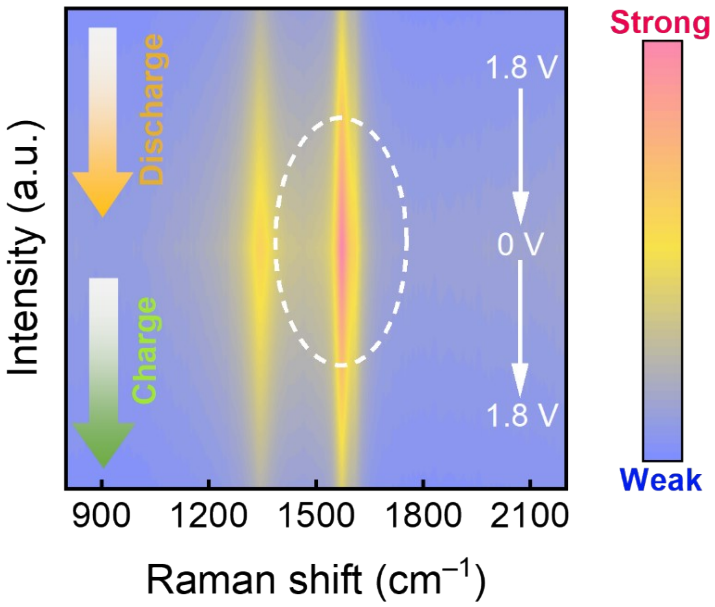

Fig. S8 *Ex-situ* Raman spectra of Fe-Na-1:2-based ZHC.

Table S4. R_s, R_{ct}, σ and $D_{Zn}^{2+}$of Fe-Na-1:2 devices in dynamic charge/discharge process.

Sample	R_s (Ω)	R_{ct} (Ω)	σ (Ω $s^{-0.5}$)	D_{Zn}^{2+} (cm^2 s^{-1})
Discharge−1.8 V	1.5	4.3	4.4	6.1×10^{-9}
Discharge−1.2 V	1.4	10.3	5.2	4.5×10^{-9}
Discharge−0.6 V	1.6	18.1	14.1	6.6×10^{-10}
Charge−0.6 V	1.3	26.6	11.2	1.4×10^{-9}
Charge−1.2 V	1.2	17.7	8.9	2.4×10^{-9}
Charge−1.8 V	1.4	11.8	5.8	1.7×10^{-8}

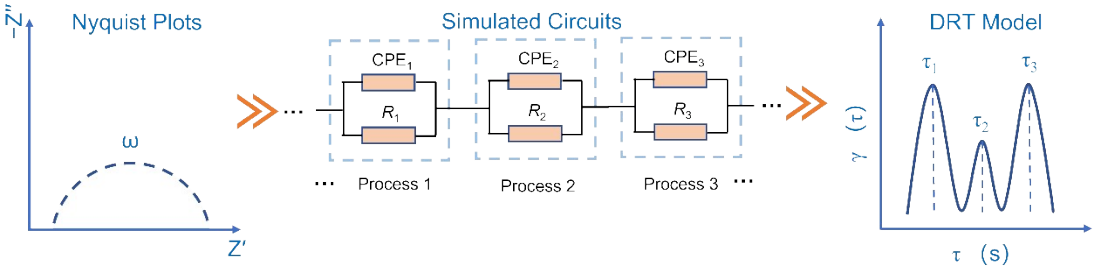

Fig. S9 Schematic of the typical impedance results shown in Nyquist plots, simulated circuit, and the DRT models. A Nyquist plot consists of a series of the paralleled RC Randles circuits, which are associated with specific DRT peaks of a specific paralleled RC circuit.

Table S5. Summary of DRT peak regions for ZHCs

DRT Peak Region	Approximate time constant τ	Assignment
τ_1	1.2 μs	Inter-particle resistance
τ_2	4.6×10^{-6}~ 0.02 s	Interfacial resistance
τ_3	0.02 ~ 0.2 s	Interfacial resistance (charge

		transfer)
τ_4	0.2 ~ 10 s	Diffusion resistance

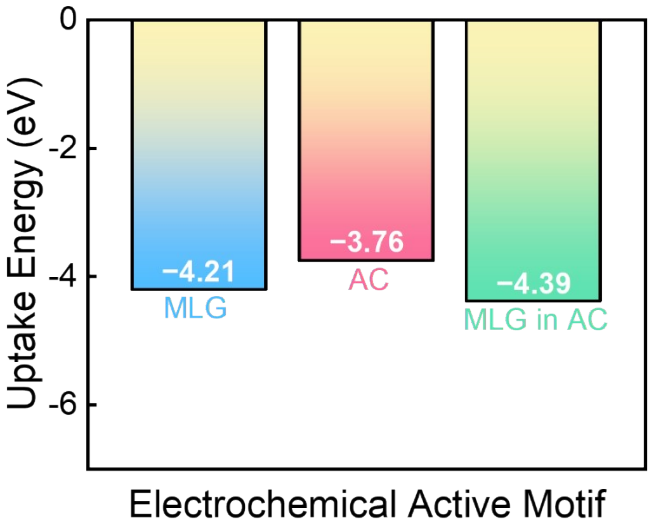

Fig. S10 The uptake energy values of single $SO_3CF_3^-$ adsorbed on the optimized redox-active sole carbonylic MLG and amorphous carbon, and synergetic MLG in amorphous carbon sites.

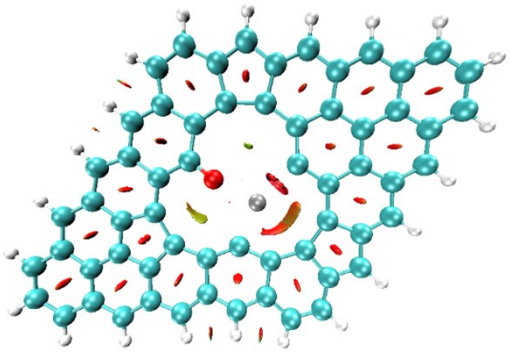

Fig. S11 Top view of the weak interaction.

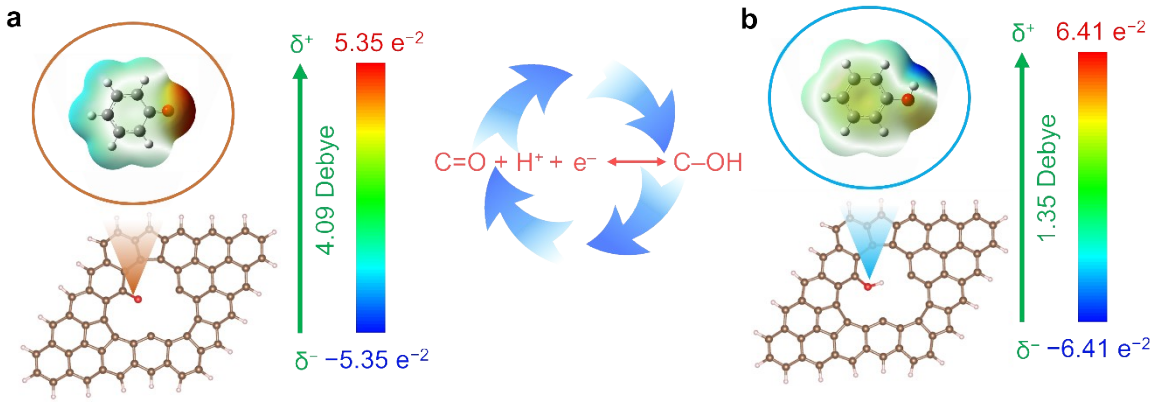

Fig. S12 Carbonylic decorated crabon frame structure transformation with H ion.

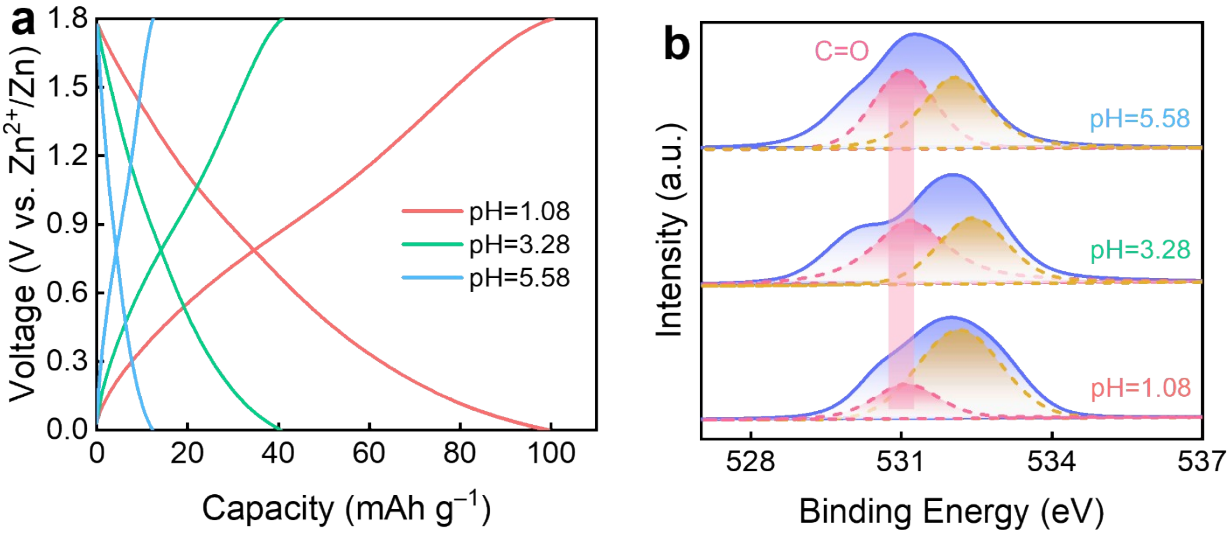

Fig. S13 (a) GCD curves at 0.5 A g^{-1} of Fe-Na cathode in HCF_3SO_3 electrolytes with different pH values and (b) corresponding high-resolution O 1s XPS spectra of Fe-Na cathodes at the fully discharged state.

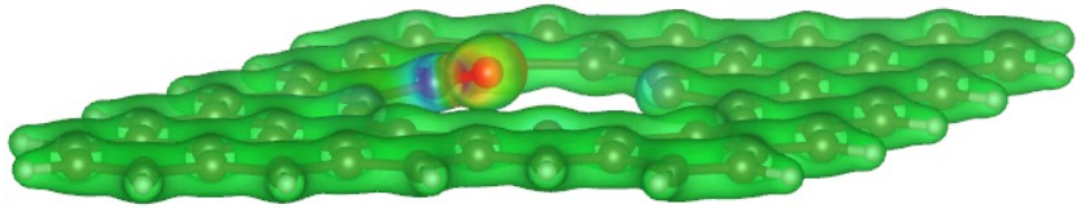

Fig. S14 Side view of the charge density of carbonylic decorated carbon frame work.

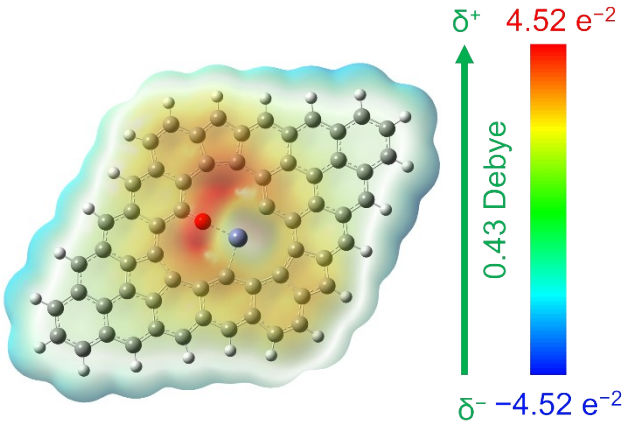

Fig. S15 Electrostatic potenial of carbonylic decorated carbon frame work with adsorbed Zn.

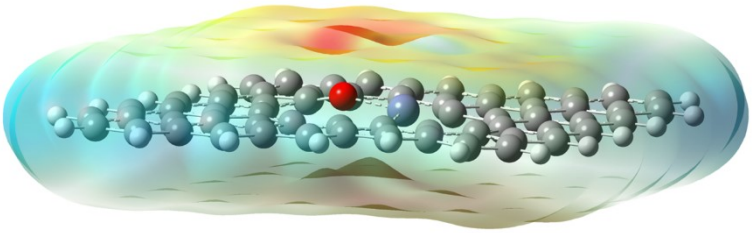

Fig. S16 Sideview of electrostatic potenial of carbonylic decorated carbon frame work with adsorbed Zn.

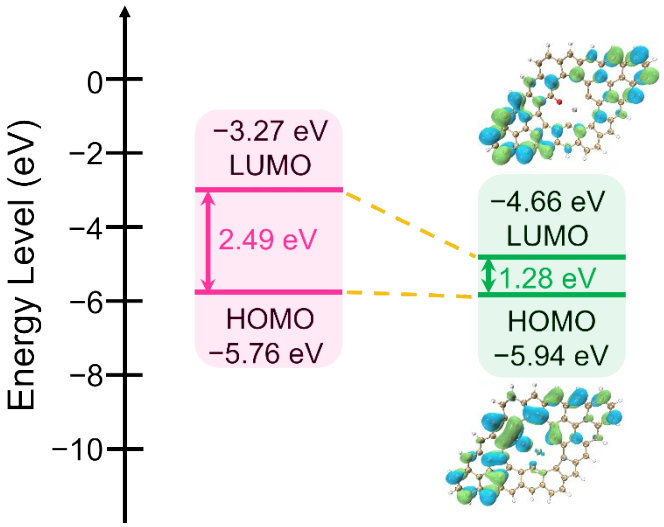

Fig. S17 Energy level of zincophilic carbon frame work before optimized and after optimized.

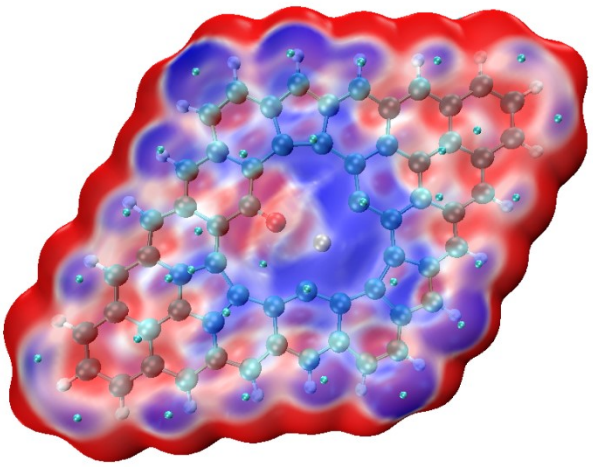

Fig. S18 Average local ionization energyies of carbon frame work with adsorbed Zn.(Cyan dots at isosurface represent extreme sites).

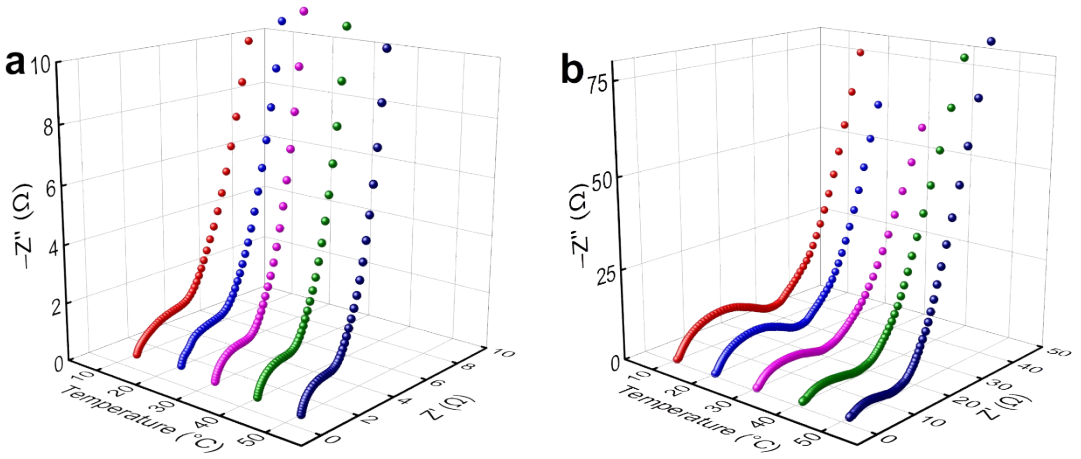

Fig. S19 EIS spectra of Fe-Na-1:2-based ZHCs at various temperatures at (a) 0.2 V and (b) 1 V.

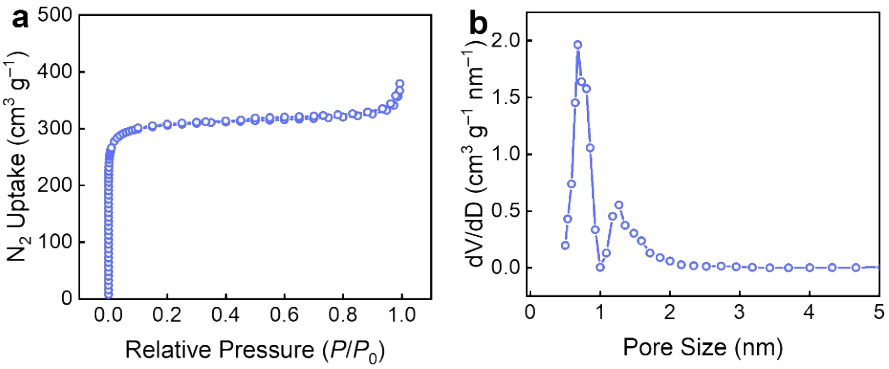

Fig. S20 (a) Nitrogen sorption isotherm and (b) corresponding pore size distribution curve of Fe-0.01 sample.

Table S6. Element contents of samples.

Samples	C (at.%)	O (at.%)	Fe (at.%)
Fe-Na-1:1	91.99	7.99	0.02
Fe-Na-1:2	90.65	9.33	0.01
Fe-Na-1:3	92.18	7.80	0.02

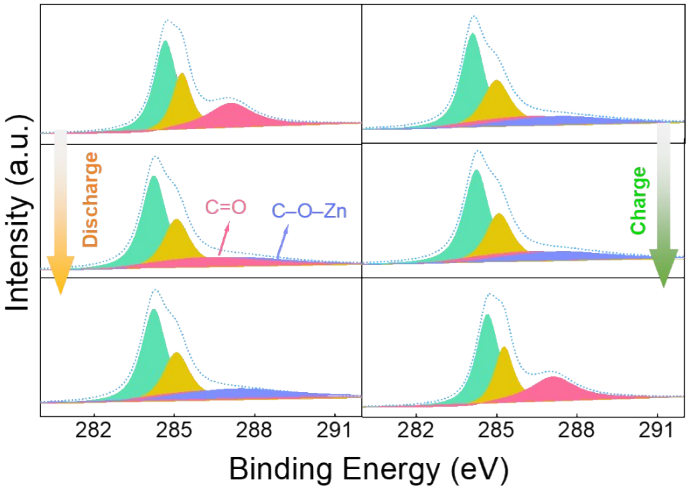

Fig. S21 High-resolution C 1s XPS spectra of Fe-Na-1:2 cathode at the fully discharged state.

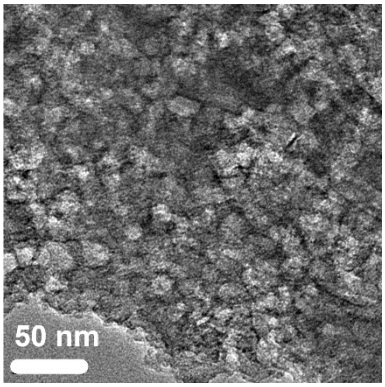

Fig. S22 Ni/Na synergism formation of carbon samples.

Reference

[S1] F. Ciuccia, C. Chen, Analysis of Electrochemical Impedance Spectroscopy Data Using the Distribution of Relaxation Times A Bayesian and Hierarchical Bayesian Approach, Electrochim. Acta 167 (2015) 439–454.

[S2] M.B. Effat, F. Ciucci, Bayesian and Hierarchical Bayesian Based Regularization for Deconvolving the Distribution of Relaxation Times from Electrochemical Impedance Spectroscopy Data, Electrochim. Acta 247 (2017) 1117–1129.

[S3] J. Liu, T.H. Wan, F. Ciucci, A Bayesian View on the Hilbert Transform and the KramersKronig Transform of Electrochemical Impedance Data: Probabilistic Estimates and Quality Scores, Electrochim. Acta 357 (2020) 136864.

[S4] T.H. Wan, M. Saccoccio, C. Chen, F. Ciucci, Influence of the Discretization Methods on the Distribution of Relaxation Times Deconvolution Implementing Radial Basis Functions with DRTtools, Electrochim. Acta 184 (2015) 483–499.

[S5] T. Lu, F. Chen, Multiwfn: A multifunctional wavefunction analyzer, J. Comput. Chem. 33 (2012) 580–592.

[S6] D. Wang, D. Lv, H. Liu, S. Zhang, C. Wang, C. Wang, J. Yang, Y. Qian, In-situ Formation of Nitrogen-Rich Solid Electrolyte Interphase and Simultaneous, Angew. Chem., Int. Ed. (2022) 202212839.

[S7] X. Qiu, N. Wang, Z. Wang, F. Wang, Y. Wang, Towards High-Performance Zinc-Based Hybrid Supercapacitors via Macropores-Based Charge Storage in Organic Electrolytes, Angew.Chem. Int. Ed. 60 (2021) 9610–9617.

[S8] C.-C. Hou, Y. Wang, L. Zou, M. Wang, H. Liu, Z. Liu, H.-F. Wang, C. Li, Q. Xu, A Gas-Steamed MOF Route to P-Doped Open Carbon Cages with Enhanced Zn-Ion Energy Storage Capability and Ultrastability, Adv. Mater. 33 (2021) 2101698.

[S9] H. He, J. Lian, C. Chen, Q. Xiong, C.C. Li, M. Zhang, Enabling Multi-Chemisorption Sites on Carbon Nanofibers Cathodes by an In-situ Exfoliation Strategy for High-Performance Zn–Ion Hybrid Capacitors, Nano-Micro Lett. 14 (2022) 106.

[S10] J. Yin, W. Zhang, W. Wang, N.A. Alhebshi, N. Salah, H.N. Alshareef, Electrochemical Zinc Ion Capacitors Enhanced by Redox Reactions of Porous Carbon Cathodes, Adv. Energy Mater. 10 (2020) 2001705.

[S11] N. Chang, T. Li, R. Li, S. Wang, Y. Yin, H. Zhang, X. Li, An aqueous hybrid electrolyte for low-temperature zinc-based energy storage devices, Energy Environ. Sci. 13 (2020) 3527--3535.

[S12] X. Shi, H. Zhang, S. Zeng, J. Wang, X. Cao, X. Liu, X. Lu, Pyrrolic-Dominated Nitrogen Redox Enhances Reaction Kinetics of Pitch-Derived Carbon Materials in Aqueous Zinc Ion Hybrid Supercapacitors, ACS Mater. Lett. 3(9) (2021) 1291−1299.

[S13] Y. Lu, Z. Li, Z. Bai, H. Mi, C. Ji, H. Pang, C. Yu, J. Qiu, High energy-power Zn-ion hybrid supercapacitors enabled by layered B/N co-doped carbon cathode, Nano Energy 66 (2019) 104132.

[S14] S. Wu, Y. Chen, T. Jiao, J. Zhou, J. Cheng, B. Liu, S. Yang, K. Zhang, W. Zhang, An Aqueous Zn-Ion Hybrid Supercapacitor with High Energy Density and Ultrastability up to 80 000 Cycles, Adv. Energy Mater. 9 (2019) 1902915.